
# Added resistance, heave and pitch for the KVLCC2 tanker using a fully nonlinear unsteady potential flow boundary element method

Ocean Engineering 229 (2021) 108935

Contents lists available at ScienceDirect

Ocean Engineering

journal homepage: www.elsevier.com/locate/oceaneng

# Added resistance, heave and pitch for the KVLCC2 tanker using a fully nonlinear unsteady potential flow boundary element method

Francesco Coslovich [a,*], Martin Kjellberg [b], Magnus Östberg [c], Carl-Erik Janson [a]

[a] Department of Mechanics and Maritime Sciences, Chalmers University of Technology, Gothenburg, SE-41296, Sweden
[b] SSPA Sweden AB, Gothenburg, Sweden
[c] Flowtech International AB, Gothenburg, Sweden

ARTICLE INFO

*Keywords:*
Fully nonlinear boundary element method
Acceleration potential
Adaptive grid refinement
KVLCC2

ABSTRACT

In this paper, a fully nonlinear unsteady potential flow method is used to predict added resistance, heave and pitch for the KVLCC2 hull in regular head waves at design speed. The method presents a nonlinear decomposition of the velocity potential and the wave field and an adaptive grid refinement. A formulation for the acceleration potential is used to obtain the pressure. To improve computational efficiency, a Barnes-Hut algorithm is introduced. A grid dependency study and a study on the impact of different time steps on the solution are performed. Numerical results have been compared with experimental data for the design speed. A general good agreement is found for added resistance, especially for longer waves. Heave and pitch are properly computed for all wave lengths in the range $\lambda/L_{pp} = 0.4$ to 1.4.

## 1. Introduction

Due to the increasing demand of transport of goods at sea across the planet and thanks to a constantly improving technology, fleet and ship sizes have been growing steadily. In order to reduce pollution in the maritime sector, the Marine Environment Protection Committee (MEPC) of the International Maritime Organization (IMO) has introduced rules to address energy efficiency of new ships. The Energy Efficiency Design Index (EEDI) has been included in those rules and it represents the carbon dioxide $CO_2$ produced per ship's capacity-mile. To estimate the $CO_2$ emitted, the operational scenario of the engine-propeller system is needed. Therefore, to obtain a reliable evaluation of the EEDI, the resistance has to be predicted with good accuracy. Historically, the power required to reach the design speed was estimated based on the evaluation of the resistance in calm water. There is an expected increase of around $15-30\%$ in the resistance when a ship is sailing in a seaway. The so called *sea margin* was applied to the power estimated from the calm water calculations, resulting in an approximately 15% larger power installed. The attention now is moving towards the evaluation of the ship performances when sailing in a seaway, without relying on an approximate approach which added a 15% to the power predicted. There are three ways to predict the performances of a ship sailing in waves: empirical methods, numerical calculations and model tests. Since model tests are quite expensive and time consuming, designers often rely on numerical methods for a large portion of the design process.

There are different types of numerical methods available to evaluate the performances of a ship sailing in a seaway. The most advanced and accurate methods used nowadays to evaluate added resistance and ship motions are based on the Unsteady Reynolds-Averaged Navier Stokes equations (URANS), see for instance el Moctar et al. (2010) or Sadat-Hosseini et al. (2013). Even though these methods can provide accurate results, they are still quite demanding in terms of computational effort. For this reason, they are not widely used during the early stages of the design process or to optimize the hull forms. More common are analytical formulations and potential flow methods.

When it comes to potential flow methods, there are several ways to evaluate the added resistance. The far-field approach was introduced by Maruo (1957) and modified in the following years by himself and by Joosen (1966). Some years later, following the method proposed by Maruo, Gerritsma and Beukelman (1972) introduced the radiated energy approach to evaluate added resistance in head waves. The so called near-field method was initially introduced by Faltinsen et al. (1980): with this method the resistance is evaluated by integrating the hydrodynamic pressure on the hull surface. In the same paper, Faltinsen proposed also a simplified formulation to obtain added resistance in short waves, where the method presented some deficiencies. The

* Corresponding author.
*E-mail address:* francesco.coslovich@chalmers.se (F. Coslovich).

https://doi.org/10.1016/j.oceaneng.2021.108935
Received 14 July 2020; Received in revised form 21 March 2021; Accepted 22 March 2021
Available online 24 April 2021

near-field method has been widely applied in recent years, with the evolution of potential flow codes towards nonlinear time domain methods. Joncquez et al. (2008) and Liu et al. (2011) computed added resistance for multiple hull forms using different 3D panel methods and applied both the far-field and near-field approaches to compare results. Joncquez used a 3D time domain high order boundary element method with Neumann-Kelvin (NK) and Double Body (DB) linearizations to compute the forces while Liu used a 3D frequency domain panel method and a hybrid time domain Rankine source-Green function method. Kim et al. (2012) computed added resistance using a time domain Rankine panel method with NK and DB linearizations, applying both the far and near-field approaches. Guha and Falzarano (2015) adopted a Green function panel method to estimate the added resistance with a near-field approach for a number of different hulls and compared the results with other numerical methods and with model tests.

In recent last years an increasing number of fully nonlinear potential flow methods have been presented. Engsig-Karup et al. (2009) developed a fully nonlinear 3D potential flow method to simulate water waves and Ducrozet et al. (2010) extended it for wave-wave and wave-structure interaction in the case of a fixed circular cylinder. Mola et al. (2017) developed a fully nonlinear potential flow method adding a pressure patch in the stern area and used it to evaluate the performances of different hulls in calm water.

In the work presented here, SHIPFLOW Motions, a fully nonlinear unsteady potential flow boundary element code based on a *Mixed Eulerian-Lagrangian* (MEL) approach, as presented in Kjellberg et al. (2011) and Kjellberg et al. (2012), is extended to include a nonlinear decomposition of the velocity potential and the wave field. A Barnes-Hut algorithm and an adaptive grid refinement scheme are introduced for computational efficiency as well as an acceleration potential approach for the pressure. This allows for a finer discretization around the hull and at areas of the free surface where a finer resolution is required. Results are presented for added resistance, heave and pitch for the KVLCC2 hull in regular head waves at design speed. Grid and time step refinement studies are included as well as comparisons with experimental results carried out at SSPA Sweden AB.

## 2. Mathematical model

### 2.1. Coordinate systems

To describe the position and the orientation of the hull and the forces acting on it, three coordinate systems are used:

- An earth-fixed right-handed coordinate system, with its origin at an arbitrary point on the initial free surface. The free surface evolution and the equations governing the flow are expressed in this system.
  •A body fixed coordinate system, with its origin at the center of gravity of the ship. This system is used to express the forces acting on the ship.
  •A body-fixed inertial coordinate system. This system is centered on the vertical line passing through the center of gravity and placed on the waterplane. It is only allowed to move on the horizontal plane and it is used to describe the motion of the ship.

### 2.2. Boundary Value Problem

In order to simulate the flow around a hull sailing in a seaway, the Navier-Stokes equation has to be solved. Since this is quite expensive in terms of computational power, a number of simplifying hypotheses can be introduced. If we assume that the fluid is homogeneous, inviscid, incompressible and irrotational, there exists a scalar quantity referred to as velocity potential φ, that describes the flow. The velocity potential is defined as:

$$\nabla\varphi = \left(\frac{\partial\varphi}{\partial x}, \frac{\partial\varphi}{\partial y}, \frac{\partial\varphi}{\partial z}\right) = (u, v, w) = \boldsymbol{u} \tag{1}$$

Substituting equation (1) into the continuity equation for incompressible fluids, we obtain Laplace's equation:

$$\nabla^2\varphi = 0 \tag{2}$$

#### 2.2.1. Free surface boundary conditions

To solve this partial differential equation, which defines the *Boundary Value Problem* (BVP), boundary conditions have to be introduced on the boundaries of the domain. On the free surface, the kinematic and dynamic boundary conditions are applied. Being $\boldsymbol{x} = (x, y, z)$ the position of a fluid particle on the free surface, the fully nonlinear kinematic and dynamic boundary conditions are, respectively:

$$\frac{D\boldsymbol{x}}{Dt} = \left(\frac{dx}{dt}, \frac{dy}{dt}, \frac{dz}{dt}\right) = (u, v, w) = \nabla\varphi \tag{3}$$

$$\frac{D\varphi}{Dt} = -gz + \frac{1}{2}\nabla\varphi\cdot\nabla\varphi - \frac{p_a}{\rho} \tag{4}$$

where $g$ is the gravitational acceleration, ρ is the fluid density and $p_a$ is the atmospheric pressure. $\frac{D}{Dt}$ is the material derivative and is defined as:

$$\frac{D}{Dt} = \frac{\partial}{\partial t} + \nabla\varphi\cdot\nabla \tag{5}$$

#### 2.2.2. Body boundary conditions

Neumann-type boundary conditions are applied on the instantaneous wetted body surface and on the bottom of the domain, imposing no flow through such surfaces, *i.e.* impermeability condition:

$$\nabla\varphi\cdot n = \frac{\partial\varphi}{\partial n} = n\cdot(\boldsymbol{u} + \boldsymbol{\omega}\times\boldsymbol{r}) \tag{6}$$

where $\boldsymbol{n}$ is the normal to the surface pointing into the fluid domain, $\boldsymbol{u}$ and $\boldsymbol{\omega}$ are the translational and angular velocities and $\boldsymbol{r}$ is the distance between the surface and the center of rotation. On the bottom an impermeability condition is applied:

$$\nabla\varphi\cdot n = 0 \tag{7}$$

### 2.3. Unsteady pressure and forces

The total pressure on the hull is given by Bernoulli's equation:

$$p = -\rho\left(\frac{\partial\varphi}{\partial t} + \frac{1}{2}\left|\nabla\varphi\right|^2 + gz\right) \tag{8}$$

The hydrodynamic forces acting on the body can then be computed by integrating the pressure over the wetted hull surface:

$$\boldsymbol{F} = -\iint_{S_b} p\,\vec{n}\,dS, \tag{9}$$

where $\boldsymbol{F} = (F_1, F_2, F_3)$ and the moments according to

$$\boldsymbol{F} = -\iint_{S_b} p(\boldsymbol{r}\times\boldsymbol{n})\,dS, \tag{10}$$

where $\boldsymbol{F} = (F_4, F_5, F_6)$.

### 2.4. Acceleration potential

The partial time derivative of the velocity potential $\frac{\partial\varphi}{\partial t}$ appears in the unsteady Bernoulli equation. This term can be obtained using a backward difference scheme if the rigid body motions is known. However, for a free floating body, this typically causes problems with stability. One

way of getting around this is to directly calculate $\frac{\partial \varphi}{\partial t}$ from its boundary conditions, as proposed by Kang and Gong (1990).

This method is based on a modal decomposition of the rigid body acceleration components, which implies the solution of $n+1$ additional BVP where $n$ is the number of degrees of freedom of the rigid body.

### 2.5. Nonlinear decomposition

To increase the efficiency of the computations, a nonlinear decomposition of the solution, as described by Ducrozet et al. (2010), is adopted. The free surface elevation ζ and the velocity potential φ are decomposed into an *incident* and a *scattered* part, where the incident terms describe the undisturbed incident wave field and the scattered terms describe any disturbance to the incident wave field:

$$\begin{aligned} \zeta &= \zeta^I + \zeta^S \\ \varphi &= \varphi^I + \varphi^S \end{aligned} \tag{11}$$

In practice this means that for a computation with no incident wave field, i.e. calm water, the incident wave elevation ($\zeta^I$) and the incident velocity potential ($\varphi^I$) are zero and the total solution is represented fully by the scattered part. In the presence of an incident wave field, $\zeta^S$ and $\varphi^S$ contain the disturbance by the hull and the effects of the interactions between this disturbance and the incident wave field.

The decomposition results in a new formulation of the free surface boundary conditions:

$$\frac{D\boldsymbol{x}}{Dt} = \nabla\left(\varphi^I + \varphi^S\right) \tag{12}$$

$$\frac{D\varphi}{Dt} = -gz + \frac{1}{2}\nabla\left(\varphi^I + \varphi^S\right)\cdot\nabla\left(\varphi^I + \varphi^S\right) - \frac{p_a}{\rho} \tag{13}$$

Since the incident wave field is a solution to the Laplace problem, the Laplace problem for the scattered solution becomes:

$$\begin{aligned} &\nabla^2\varphi^S = 0, \quad \boldsymbol{x} \in D \\ &\varphi^S = \varphi - \varphi^I, \quad \boldsymbol{x} \in S_f \\ &\nabla\varphi^S\cdot\boldsymbol{n} = (\boldsymbol{v} + \boldsymbol{\omega}\times\boldsymbol{r})\cdot\boldsymbol{n} - \nabla\varphi^I\cdot\boldsymbol{n}, \quad \boldsymbol{x} \in S_b \end{aligned} \tag{14}$$

for the fluid domain $D$ bounded by the free surface $S_f$ and the wetted body surface $S_b$. Note that the free surface boundary conditions (12) and (13) have to be evaluated at the total surface elevation $\zeta = \zeta^I + \zeta^S$. This means that the incident part of the potential $\varphi^I$ also has to be evaluated at the total surface elevation ζ. Also note that the free surface evolution tracking in time is done for the total solution (scattered plus incident) in order not to loose nonlinear effects.

The pressure can finally be calculated in two different ways, where the scattered part is either evaluated by means of backward-differences $\frac{\partial \varphi_D^S}{\partial t}$ or based on the acceleration potential $\frac{\partial \varphi_P^S}{\partial t}$:

$$p_D = -\rho\left(\frac{\partial \varphi^I}{\partial t} + \frac{\partial \varphi_D^S}{\partial t} + \frac{1}{2}\left|\nabla\varphi\right|^2 + gz\right). \tag{15}$$

$$p_P = -\rho\left(\frac{\partial \varphi^I}{\partial t} + \frac{\partial \varphi_P^S}{\partial t} + \frac{1}{2}\left|\nabla\varphi\right|^2 + gz\right). \tag{16}$$

## 3. Numerical method

In this section, some details of the method are discussed. Since the method is unsteady, a scheme for the integration in time has to be introduced. A fourth order Runge-Kutta is used for the first four time steps, while a fourth order Adams-Bashforth-Moulton method is adopted for the remaining part of the simulation.

### 3.1. Boundary element method

The BVP described in Section 2.2 is solved using a *Boundary Element Method* (BEM). The surface of the ship and the free surface are discretized by means of flat quadrilateral panels with an unknown constant strength source distribution. To obtain the source strength σ, the Green's function is used. Given two points $P$ and $Q$ on the domain, Green's function is defined as:

$$G = \frac{1}{4\pi r(P,Q)} \tag{17}$$

where

$$r(P,Q) = \sqrt{\left(x_P - x_Q\right)^2 + \left(y_P - y_Q\right)^2 + \left(z_P - z_Q\right)^2} \tag{18}$$

If there are only sources on the boundary of the domain, the velocity potential at a point $P$ becomes, using Green's theorem:

$$\varphi(P) = -\frac{1}{\alpha}\iint_S\left[G\frac{\partial\varphi(Q)}{\partial n}\right]dS \tag{19}$$

where $S$ is the boundary of the domain, $n$ is the normal direction of the panel, α is the solid angle and $G$ is the Green's function and represents the potential of a source. The solid angle α is equal to 1 if $P$ is inside the domain and $\frac{1}{2}$ if $P$ belongs to the boundary. For a point $P$ in the fluid domain then, the velocity potential is:

$$\varphi(P) = -\frac{1}{4\pi}\iint_S\left[\frac{1}{r(P,Q)}\sigma(Q)\right]dS \tag{20}$$

### 3.2. Free surface evolution

In the formulation described above, the time dependency is introduced by the fully nonlinear boundary conditions on the free surface. The evolution in time of the free surface is obtain with a *mixed Eulerian-Lagrangian* (MEL) approach, introduced by Longuet-Higgins and Cokelet (1976), using markers tracing the free surface and its velocity potential. With this methodology, each step is divided into two sub-steps:

1. Eulerian step: the BVP is solved by means of the BEM. At the end of this step the velocity potential and velocity at the markers are calculated.
2. Lagrangian step: the free surface boundary conditions defined in Equations (21) and (22) are integrated in time and the position of the markers is updated.

Once the Lagrangian step is finished, a new free surface mesh is generated by interpolating the surface elevation. In addition, the boundary conditions for the next Eularian step are obtained by interpolating the velocity potential of the markers.

The interpolation can handle sets of structured or unstructured points. By enforcing a single-valued free surface, thin-plate splines can be used for this purpose.

### 3.3. Damping zone

In order to avoid unwanted reflection from the domain boundaries, a damping zone is introduced. The damping zone ensures that the solutions from the inner and outer domain match at the intersection. Due to the presence of a body in the inner domain, the velocity potential is expected to be different, compared with the outer domain, which is known *a priori*. The damping zone phases out this difference introducing a damping term in the free surface boundary conditions for the extension of the damping zone:

$$\frac{D\boldsymbol{x}}{Dt} = \nabla\left(\varphi^I + \varphi^S\right) - \nu\boldsymbol{x}_{\text{damp}} \tag{21}$$

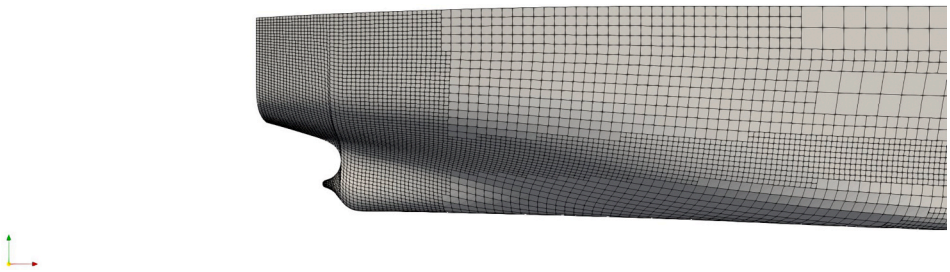

**Fig. 1.** Mesh resolution for KVLCC2.

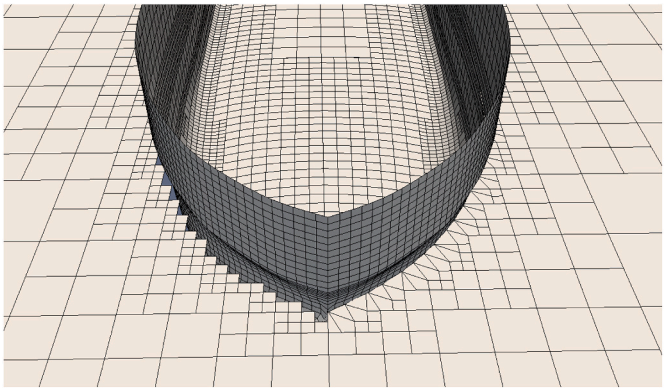

**Fig. 2.** Detail of the intersection between free surface and the hull before and after the stretching.

$$\frac{D\varphi}{Dt} = -gz + \frac{1}{2}\nabla\left(\varphi^I + \varphi^S\right)\cdot\nabla\left(\varphi^I + \varphi^S\right) - \frac{p_a}{\rho} - \nu\varphi_{\text{damp}} \tag{22}$$

where $\nu$ is a damping factor based on a quadratic function of the generalised space variable $s$:

$$\nu(s) = \begin{cases} 0 & \text{for } s \le s_0 \\ \mu(s - s_0)^2 & \text{for } s > s_0 \end{cases} \tag{23}$$

in which $s_0$ marks the beginning of the artificial damping zone and $\mu$ is a tuning factor. Due to the decomposition of the velocity potential, the damping function is only applied to the scattered part and is expressed as

$$\begin{aligned} \boldsymbol{x}_{\text{damp}} &= \left(0, 0, \zeta^S\right) \\ \varphi_{\text{damp}} &= \varphi^S \end{aligned} \tag{24}$$

### 3.4. Free surface mesh generation

The code presented here uses an automatic unstructured free surface mesh generation. The mesh generator, which is embedded in the code, re-evaluates the free surface at the end of each Lagrangian step. The body is meshed before the first time step only. The domain is discretized with quadrilateral panels of varying dimensions, following the scheme presented in Section 3.4.1.

#### 3.4.1. Adaptive mesh refinement

To increase efficiency and accuracy of the computations, an adaptive mesh refinement is used. This is also possible thanks to the decomposition of the velocity potential, which allows for a coarser discretization away from the bodies. The adaptive mesh refinement is applied on the free surface, while on the hull the panelization is kept constant during a simulation. An initial refinement is applied on the hull too, based on local curvature. Furthermore, a refined band on panels is added around the waterline and on the bow and stern. An example of the refinement around the stern for the KVLCC2 can be seen in Fig. 1.

On the free surface instead, an adaptive refinement scheme is used at each time step if a criterion is met. Every time a criterion is met for a panel, this is split recursively into four sub-panels. The user specifies a maximum level of refinement which represents the maximum number of subdivisions a panel can go through. There are two criteria that trigger the refinement: one is connected with the intersection between the free surface and the hull and the second one is based on the curvature of the scattered free surface elevation $\zeta^S$. Regardless of the criterion though, there will never be two neighboring panels with more than one level difference between the two. On the intersection between the free surface and the hull, the panels have the maximum level of refinement. Moving away from the hull, the levels are linearly decreased. It can happen that when a panel is split into its four sub-panels due to the presence of the hull, one of these can end up being completely inside the hull. This sub-panel will then be discarded and the refinement will continue on those cut by the intersection between free surface and the hull. Since the domain is discretized by quadrilateral panels, at the end of this process there will still be gaps between the free surface and the hull, even for the maximum level of refinement. To get rid of these gaps, the hanging nodes of the panels closest to the hull are stretched until the waterline. The nodes can be stretched along a grid line or diagonally. The direction $\boldsymbol{d}_s$ for the stretching is chosen to avoid overlaps with neighboring panels. The panel $p$ on the body closest to the hanging node $n$ is used to evaluate the distance $d$ the node has to be stretched for. The algorithm then moves the node along $\boldsymbol{d}_s$ for a fraction of $d$ until the node is on the hull. The comparison of the intersection between the hull and the free surface before and after the stretching can be seen in Fig. 2.

As far as the criterion on the curvature is concerned, the refinement is triggered if the curvature between two control points in the vertical plane exceeds a fixed value. In this way, it is possible to have a coarse representation of the incoming waves and have a finer mesh on the waves generated by the hull. A comparison between the initial time step with the hull at rest and the final one with the generated waves for the KVLCC2 in calm water can be seen in Fig. 3. Since the method is fully nonlinear, it means that the boundary conditions have to be applied on the exact free surface location. To satisfy this requirement, the mesh generator and consequentially the refinement scheme are called at each sub-time step of the Adam-Bashforth-Moulton method.

### 3.5. Barnes-Hut algorithm

In order to further decrease the computational effort, a Barnes-Hut algorithm, presented by Barnes and Hut (1986), is used. Thanks to this algorithm, the computational effort needed to solve BVP decreases from $O(n^2)$ to $O(n\log(n))$. With this algorithm, panels are grouped together in nodes based on the distance of an area of interest. When the BVP is solved, the panels belonging to one node are treated as a single panel. Furthermore, the further away the node is from the point of interest, the smaller the influence of the node on it. Grouping more panels into a single node will result in a faster computation at the expenses of the accuracy. This can be controlled by the user, specifying the ratio between the dimensions of a node, *i. e.* how many panels it contains, and the distance at which the influence of the node fades away. The Barnes-Hut algorithm was initially introduced to deal with astrophysics

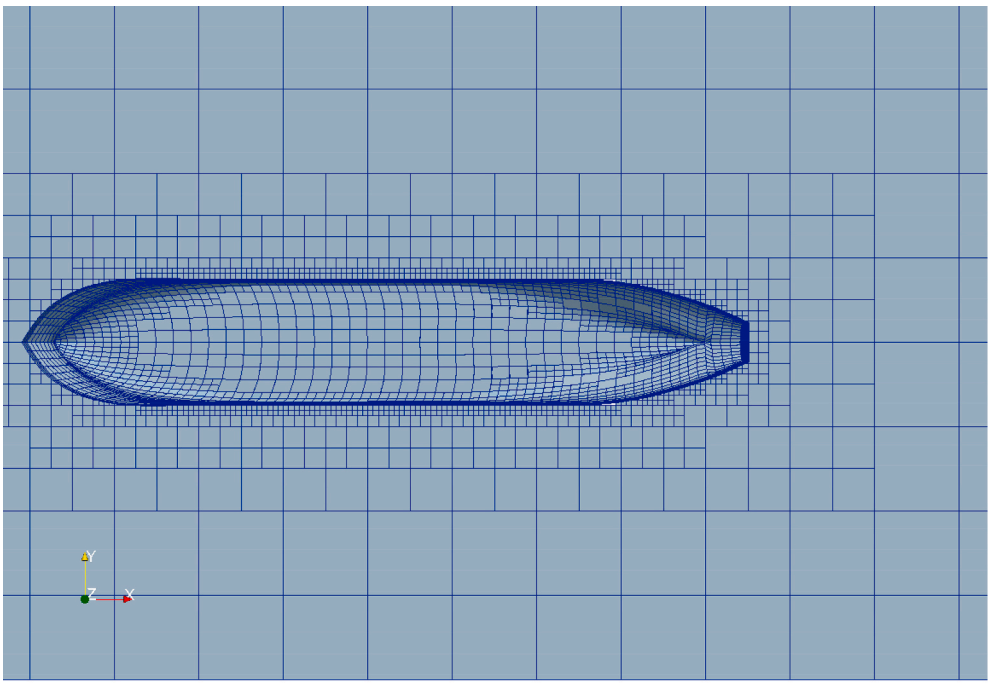

(a)

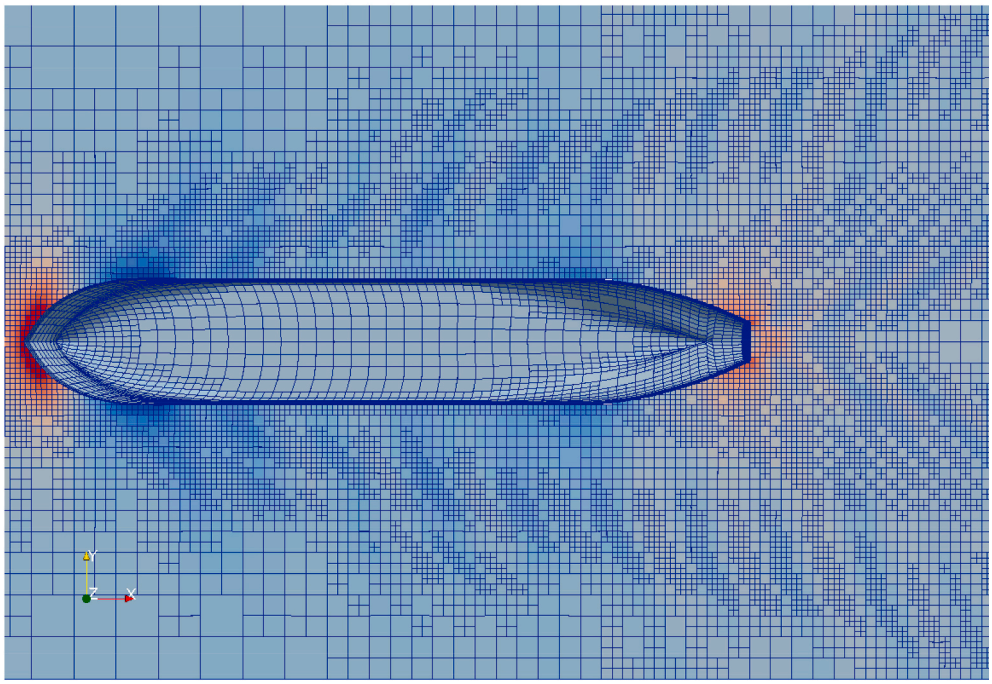

(b)

**Fig. 3.** Comparison between initial and final mesh with the adaptive mesh refinement.

simulations, where the influence of gravity decreases with $\frac{1}{r^2}$. Since the influence of the velocity potential varies with a $\frac{1}{r}$ function, some problems in accuracy can arise. To deal with this problem, a multipole expansion method is adopted.

## 4. Simulations setup

In this section a description of the setup of the numerical simulations is given. A more detailed insight about the mesh resolution on the free surface and what different levels mean will be given in Section 5. The hull used for this study is the KVLCC2 tanker and the numerical results are compared with the experimental tests carried out at SSPA Sweden AB. The ship has been tested at the design speed of 15.5 *kn* in head waves for wave lengths going from $\lambda = 0.4 \cdot L_{pp}$ to $\lambda = 1.4 \cdot L_{pp}$ with 0.1 interval. The main particulars of the ship are given in Table 1. The scale factor is $\lambda = 68$.

To properly replicate the conditions of the towing tank, the body hull is towed using a set of springs. The stiffness of the springs is the same of

**Table 1**
Ship particulars.

| | |
|---|---|
| $L_{pp}$ | 320.0 $m$ |
| $B$ | 58.0 $m$ |
| $T$ | 20.8 $m$ |
| $C_b$ | 0.810 |
| $\nabla$ | 312622 $m^3$ |
| *Design speed* | 15.5 $kn$ |
| *Fn* | 0.142 |

those used in the towing tank. At the beginning of the simulation, the ship is at rest. To have a smooth transition from rest to the prescribed speed, an acceleration ramp is imposed to keep the transient as little as possible.

The discretized domain is set as follow: it extends for $3L_{pp}$ upstream and $3L_{pp}$ downstream from the centerplane of the ship and for $2L_{pp}$ sidewards. The domain and the extension of the damping zone can be seen in Fig. 4. In the figure it is possible to see the variation of the strength of the damping factor $\nu(s)$, as presented in Section 3.3, from zero in the vicinity of the hull to its maximum value on the domain boundaries. Since only calm water and head waves are simulated, a symmetry condition is applied on the longitudinal plane.

The length of the simulations is set in order to have a number of encounter periods between the ship and the incoming waves which ensures a convergence in the forces. The number of encounter periods goes from a maximum of 100 for $\lambda = 0.4{\cdot}L_{pp}$ to a minimum of 44 for $\lambda = 1.4{\cdot}L_{pp}$. The time step is set in relation to the fundamental wave period of the steady generated waves, calculated based on the Froude number. For the grid dependency described in Section 5 the time step is set equal to 30 time steps per fundamental period. A more detailed description of the time stepping and the investigation on how this affects the solution is presented in Section 6.

The incoming waves replicate the ones tested in the model basin. The wave steepness $s_w = h_w/\lambda$ is equal to 0.02 for wave lengths up to $\lambda \leq 0.9{\cdot}L_{pp}$ and 0.01 for longer waves. Due to the depth of the tank, a deep water condition can be assumed for waves no longer than $\lambda = 1.4{\cdot}L_{pp}$.

## 5. Grid convergence

A grid dependency study has been carried out to find the best compromise between accuracy and computational time. This study focuses on the resolution of the free surface, while the mesh on the hull is the same for all the cases. As mentioned in Section 3.4, the mesh on the hull is refined around the intersection with the waterplane and around high flared areas. For this study, a total number of approximately 5.3k panels are used to discretize half of the hull. The hull can be seen in Fig. 5, and has the same mesh for all simulations.

**Table 2**
Different combinations of levels of refinement tested on the free surface. Group a represents the same level of refinement on the free surface and on the waterline; group b is the variation on the free surface only; group c shows the variation of the initial base grid, while the refinement are kept constant.

| | ID | Levels | | Panels Calm Water | | |
|---|---|---|---|---|---|---|
| | | WL | Curv. | Initial | Final | WL |
| a | 1 | 4 | 4 | 580 | 1100 | 50 |
| | 2 | 5 | 5 | 715 | 2700 | 95 |
| | 3 | 6 | 6 | 1255 | 5900 | 190 |
| b | 4 | 6 | 4 | 1255 | 1760 | 190 |
| | 5 | 6 | 5 | 1255 | 3200 | 190 |
| | 6 | 6 | 6 | 1255 | 5900 | 190 |
| c | 7 | 6 | 6 | 745 | 3750 | 135 |
| | 8 | 6 | 6 | 1255 | 5900 | 190 |
| | 9 | 6 | 6 | 1680 | 8000 | 270 |

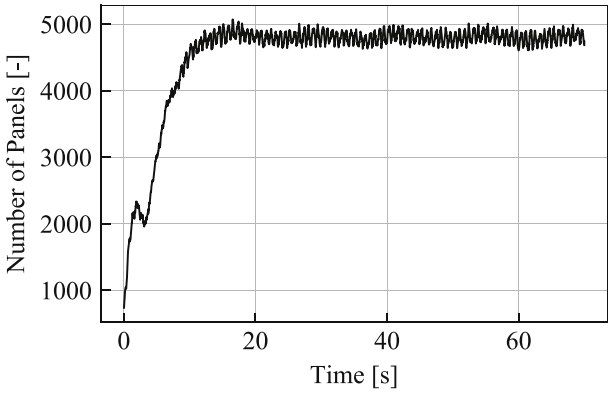


**Fig. 6.** Variation in time of the number of panels on the free surface for case 2 with $\lambda = 1.2\,L_{pp}$ and $Fn = 0.142$.

**Fig. 4.** Simulation domain with damping zone.

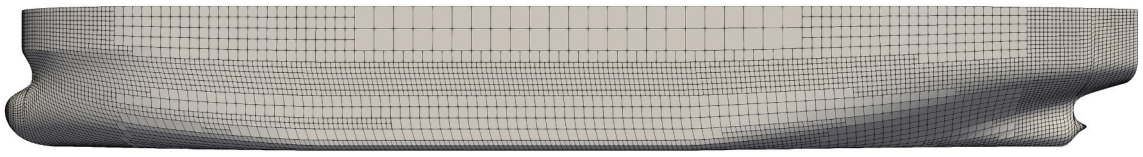

**Fig. 5.** Mesh resolution on the hull.

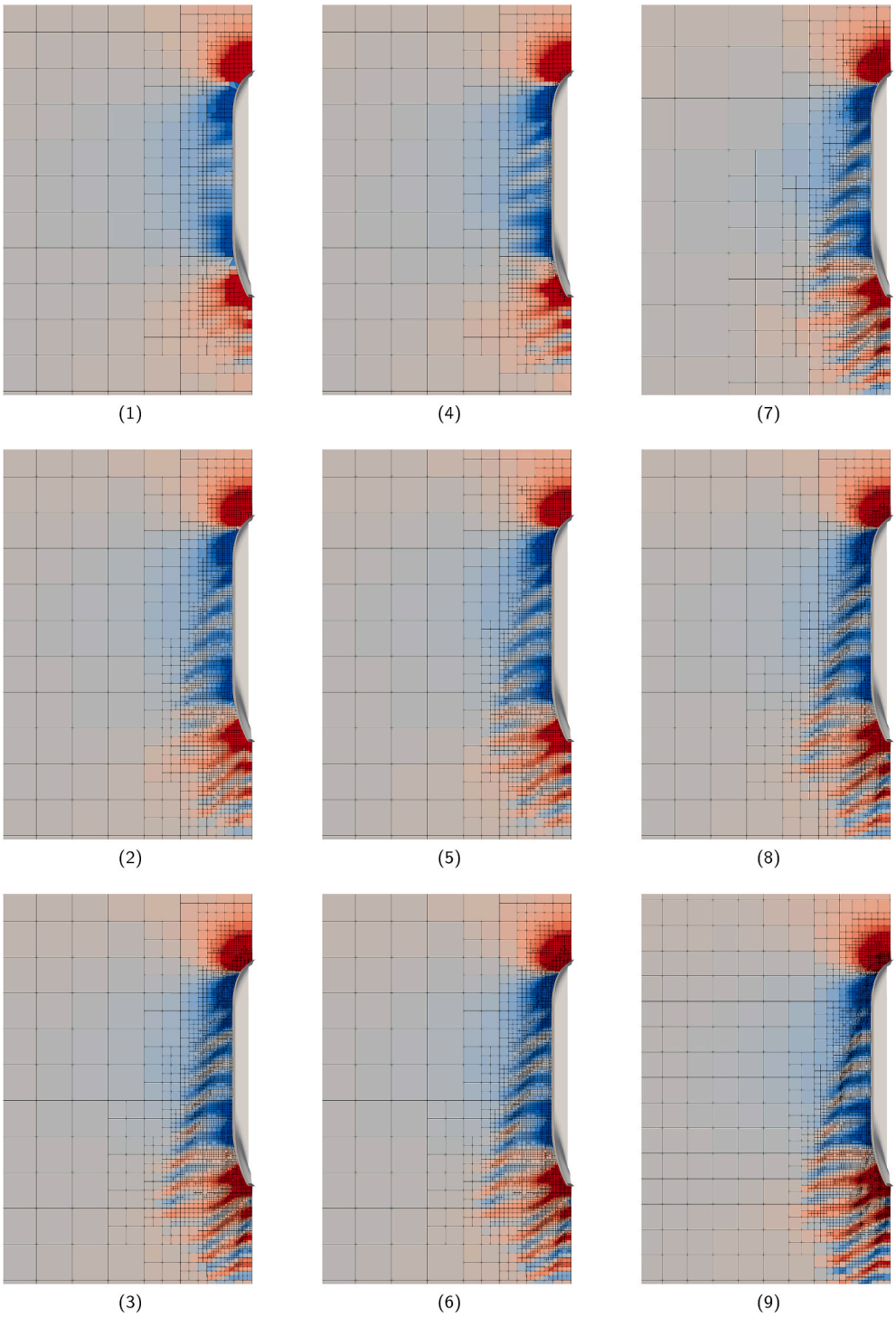


**Fig. 7.** Grid levels for the 9 cases listed in Table 2 at the final time step in calm water for $Fn = 0.142$.

### 5.1. Definition of the cases

As far as the free surface is concerned, both criteria that trigger the refinement are varied and analyzed separately. In Table 2 an overview of the different settings is provided: initially, the same maximum level of refinement is kept on the intersection between the free surface and the hull and on the curvature of the free surface. These cases correspond to group *a*, IDs 1, 2 and 3 in the table. Note that it is not possible to have a higher resolution on the free surface based on the curvature than around the waterplane. Afterward, for group *b*, cases 4, 5 and 6, the level around the hull is kept constant and the level on the curvature is varied: in this way, since the mesh around the hull does not change, it is possible to analyze the influence of the resolution of the generated waves on the solution. Throughout this study, the initial base grid is the same. The number of panels with a level zero of refinement in $x$ and $y$ direction are 36 and 12 respectively. The last part of the grid convergence analysis consisted in varying the base grid, corresponding to cases 7, 8 and 9, group *c*, in the table. Compared to the reference case, the size of the area of the panels of the base grid was varied with a factor of 2.

**Table 3**
Number of panels per fundamental wave length.

| | ID | Panels per wave | |
|---|---|---|---|
| | | @ waterline | wave cut @ $y = 0.15L_{pp}$ |
| a | 1 | 6.4 | 10.7 |
| | 2 | 12.1 | 20.2 |
| | 3 | 24.2 | 29.1 |
| b | 4 | 24.2 | 11.2 |
| | 5 | 24.2 | 20.7 |
| | 6 | 24.2 | 29.1 |
| c | 7 | 17.2 | 26.2 |
| | 8 | 24.2 | 29.1 |
| | 9 | 34.4 | 32.5 |

### 5.2. Calm water

To summarize, the study can be divided into three steps as can be seen in Table 2. In the table it is also possible to see the initial and final number of panels on the free surface in calm water and the number of panel along the waterline (WL). Note that cases 3, 6 and 8 represent the same condition. A visual representation of the calm water simulations, with a fully developed wave system, can be seen in Fig. 7. Due to the adaptive grid refinement, the number of panels for each simulation varies in time. Since the ship starts at rest, there is no refinement at the initial time step due to the curvature of the free surface. As the ship reaches the prescribed speed, the number of panels will increase and it will oscillate around a mean value. In Fig. 6 it is possible to see the time series of the number of panels for the case 2 in waves with wave length $\lambda = 1.2{\cdot}L_{pp}$.

It can be relevant to compare the number of panels per fundamental wave length as well. The fundamental wave length is calculated as $\lambda = 2\pi Fn^2 L$. The number of panels per fundamental wave length is obtained on the waterline and on a longitudinal wave cut at $y = 0.15{\cdot}L_{pp}$, $2{\cdot}L_{pp}$ long which starts $0.25{\cdot}L_{pp}$ forward of the fore perpendicular and pointing downstream. The values for the different cases are reported in Table 3. Since cases 3, 4, 5, 6 and 8 have the same refinement on the intersection between the hull and the free surface, they have the same number of panels per wave length.

### 5.3. Head waves

To analyze the convergence of different meshes and find a compromise between accuracy and computational time, the cases listed in Table 2 were tested with incoming head waves. To assess the convergence, added resistance coefficient and non-dimensional heave and pitch were compared. The added resistance $R_{AW}$ in head waves is defined as the difference between the resistance in waves $R_w$ and the resistance in calm water $R_c$. The added resistance coefficient is defined as:

$$CAW = \frac{R_{AW}}{\rho g A^2 B^2 / L_{pp}} \tag{25}$$

Being $B$ the breadth of the ship and $A$ the wave amplitude. Heave and pitch are nondimensionalized with wave amplitude and wave slope respectively.

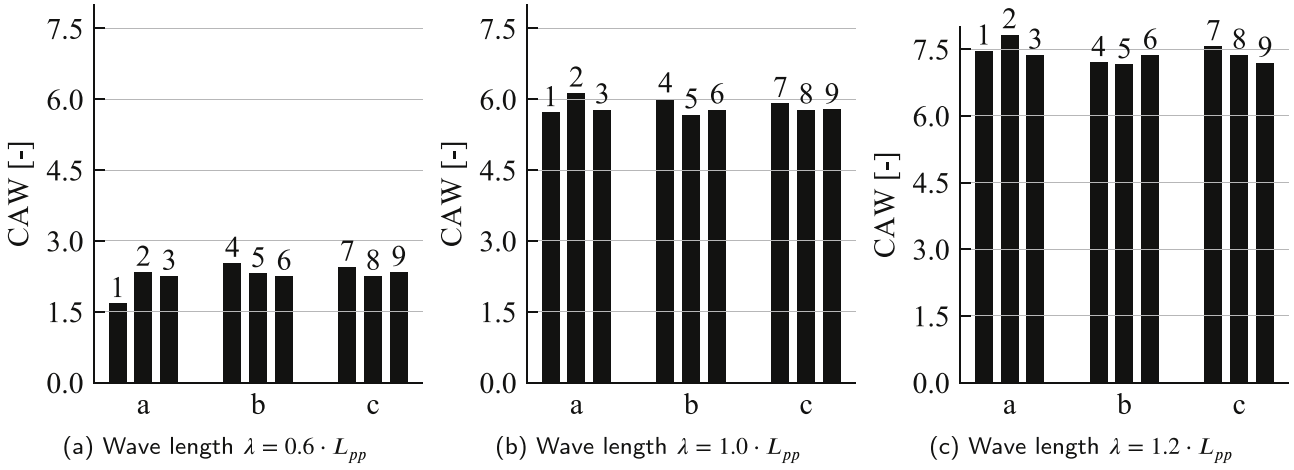


**Fig. 8.** Variation of added resistance coefficient for the different cases for three wave lengths at $Fn = 0.142$.

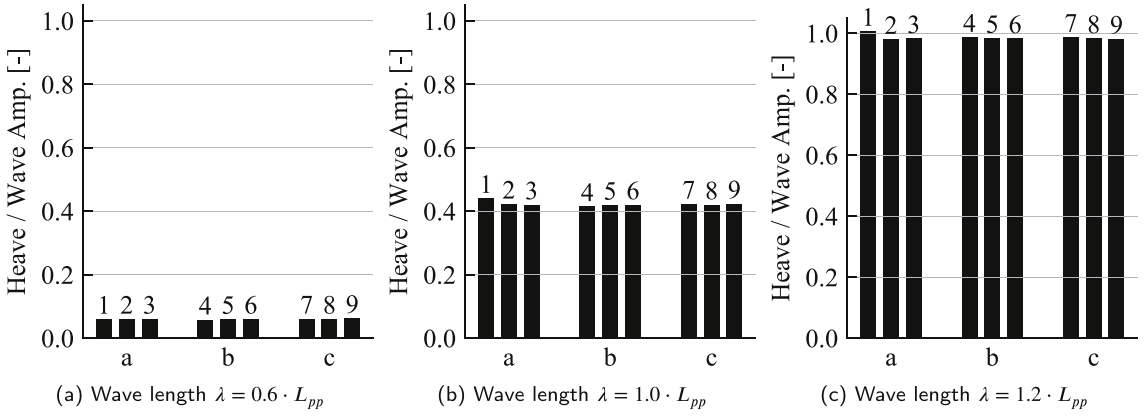


**Fig. 9.** Variation of heave for the different cases for three wave lengths at $Fn = 0.142$.

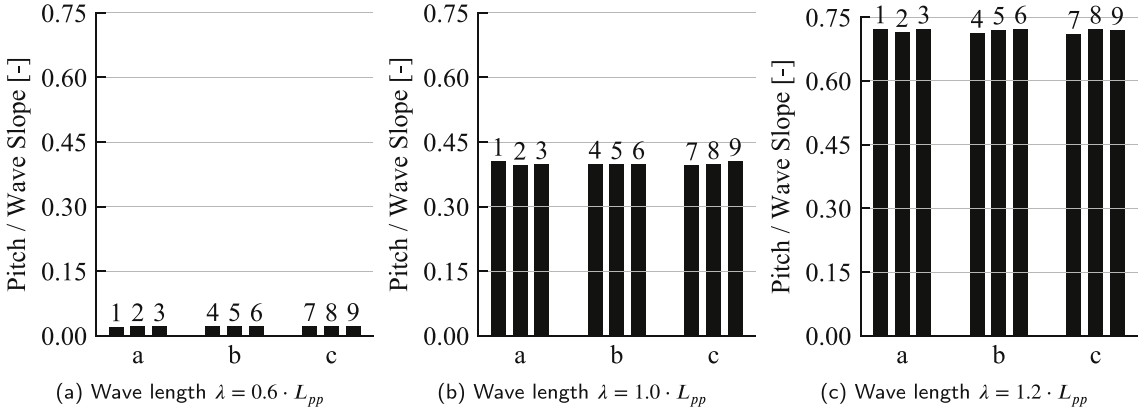


**Fig. 10.** Variation of pitch for the different cases for three wave lengths at $Fn = 0.142$.

**Table 4**
Computational time for different cases at $Fn = 0.142$.

| | ID | $\lambda = 0.6\,L_{pp}$ | | $\lambda = 1.2\,L_{pp}$ | |
|---|---|---|---|---|---|
| | | $T_c$ | $T_c$ per $T_e$ | $T_c$ | $T_c$ per $T_e$ |
| a | 1 | 6.5h | 0.09h | 6.8h | 0.14h |
| | 2 | 14h | 0.19h | 14.5h | 0.30h |
| | 3 | 37.3h | 0.49h | 41h | 0.84h |
| b | 4 | na | na | na | na |
| | 5 | 19.3h | 0.25h | 19.3h | 0.39h |
| | 6 | 37.3h | 0.49h | 41h | 0.84h |
| c | 7 | 20.3h | 0.27h | 20.8h | 0.43h |
| | 8 | 37.3h | 0.49h | 41h | 0.84h |
| | 9 | 68h | 0.64h | 94h | 1.69h |

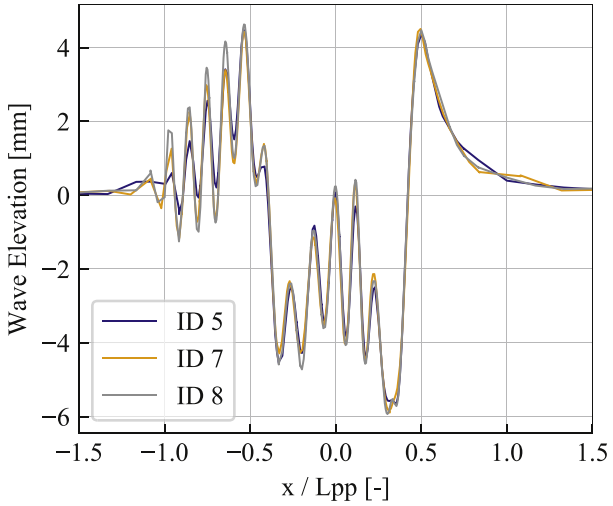


**Fig. 11.** Wave cut at $y = 0.15 \cdot L_{pp}$ for IDs 5, 7 and 8 for the calm water case at $Fn = 0.142$.

In Fig. 8, the variation of the added resistance coefficient with the number of panels in waves for wave lengths $\lambda = (0.6,\ 1.0,\ 1.2) \cdot L_{pp}$ can be observed. In Figs. 9 and 10, the influence of the number of panels on heave and pitch can be seen for the same wave lengths. Since the total number of panels on the free surface varies with time, an average value of the tail of the simulation is taken. As can be seen, the variation for the motions is very limited while bigger discrepancies are found for the added resistance coefficient. Nevertheless, the biggest discrepancies for added resistance can be seen for case 1, 2 and 4. These cases represent the coarsest resolutions and, for cases 1 and 2, there are not enough panels around the waterline to properly resolve the forces acting on the hull.

The other important aspect to keep in mind when selecting the mesh resolution is the computational time needed to run the simulations. In Table 4 the computational time $T_c$ for the different cases is reported for some of the wave lengths. The computations were run on 4 cores on an Intel i7-7700K CPU @ 4.20 GHz. In the table the computational time per wave encounter is also presented. This value represents an average: is obtained dividing the total computational time with the number of encounter periods. The case with ID number 4 was not run on the same computer, therefore the time is not reported.

### 5.4. Selection

Combining the information given in Figs. 8–10 on the convergence of the forces with the one in Table 4, we can say the best compromise between accuracy and computational effort is given by cases 5 and 7. Although cases 3, 6 and 8, which represent the same condition, provide closer results to case 9, which is the finest mesh, they require higher computational time compared to cases 5 and 7. In order to select a case between 5 and 7, it is worth to look at contour plots and at a wave cut for the calm water simulations. The wave cuts at $y = 0.15 \cdot L_{pp}$ are shown in Fig. 11 and the contour plots in Fig. 12. As can be seen, case 7 gives closer results in terms of wave cut to case 8, as well as a slightly better resolved wave system. Therefore, case 7 is selected for the comparison with experimental results.

## 6. Time step dependency

After the grid dependency was performed, a grid resolution was selected for the comparison with the experimental data. The case selected for the comparison is case 7, as discussed in Section 5.4. After a quick comparison with the experimental data, it was observed that a further investigation was needed for the short waves range. Before proceeding with the comparison with the experimental results then, the influence of the time step on the solution was investigated.

As mentioned in Section 4, the time step for the simulations is based on the fundamental wave length $\lambda = 2\pi Fn^2 L$. For the grid dependency, a number of 30 time steps per fundamental wave period was chosen. For this investigation, three more values were selected: 15, 45 and 60 steps per fundamental wave period. Since the value of the time step and the length of the simulations are the same for all the wave lengths, the number of time steps per encounter period will vary for the different cases. In Table 5, the number of time steps per encounter period can be observed for different wave lengths for all the cases.

The added resistance coefficient was evaluated for different wave lengths using different time step sizes. The wave lengths used range from $\lambda = 0.4 \cdot L_{pp}$ to $\lambda = 0.9 \cdot L_{pp}$. In Fig. 13 the added resistance coefficient is

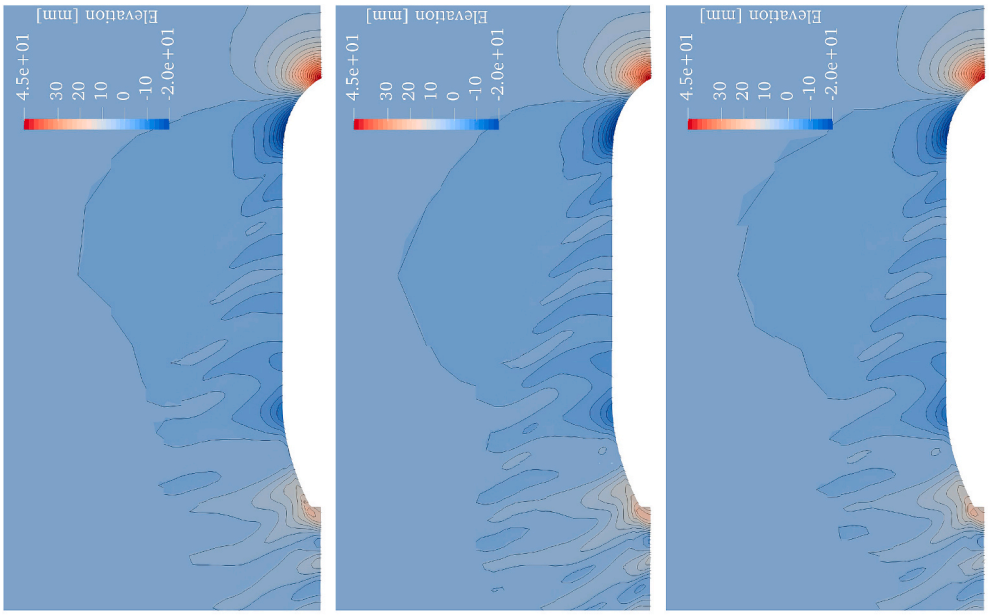


(a) Case 5 (b) Case 7 (c) Case 8

**Fig. 12.** Contour plots for the calm water case for IDs 5, 7 and 8 at $Fn = 0.142$.

**Table 5**
Number of time steps per encounter period for the different cases for $Fn = 0.142$.

| $\lambda/L$ | time steps per $T_e$ | | | |
|---|---|---|---|---|
| | N steps 15 | N steps 30 | N steps 45 | N steps 60 |
| 0.4 | 18 | 35 | 53 | 71 |
| 0.5 | 21 | 41 | 62 | 82 |
| 0.6 | 23 | 47 | 70 | 93 |
| 0.7 | 26 | 51 | 77 | 103 |
| 0.8 | 28 | 56 | 84 | 112 |
| 0.9 | 30 | 60 | 91 | 121 |
| 1.0 | 32 | 65 | 97 | 129 |
| 1.1 | 34 | 69 | 103 | 137 |
| 1.2 | 36 | 73 | 109 | 145 |
| 1.3 | 38 | 76 | 114 | 152 |
| 1.4 | 40 | 80 | 120 | 160 |

shown. Contour plots for $\lambda = 0.5 \cdot L_{pp}$ for the different cases are shown in Fig. 14.

There are two main points that can be highlighted from Fig. 13: first of all, there is a clear convergence increasing the number of steps per fundamental period. Although the contour plots of Fig. 14 seem quite similar, the difference in the added resistance coefficient is not negligible, especially for shorter waves. Furthermore, the relative difference between the four cases diminishes with increasing wave length. As reported in Seo et al. (2014), in short waves nonlinearities play an important role in the evaluation of added resistance. Since the code used here assumes fully nonlinear boundary conditions and the forces are obtained from the direct integration of the nonlinear pressure on the hull surface, the discrepancies in the short waves range could be mainly due to an insufficient number of time steps for these cases, as can be seen in Table 5.

The case selected for the comparison with experimental results is the one with 45 steps per fundamental wave period. As can be seen for Fig. 13, the difference between this case and the case with 60 steps is very small. Furthermore, there is a significant change in computational time.

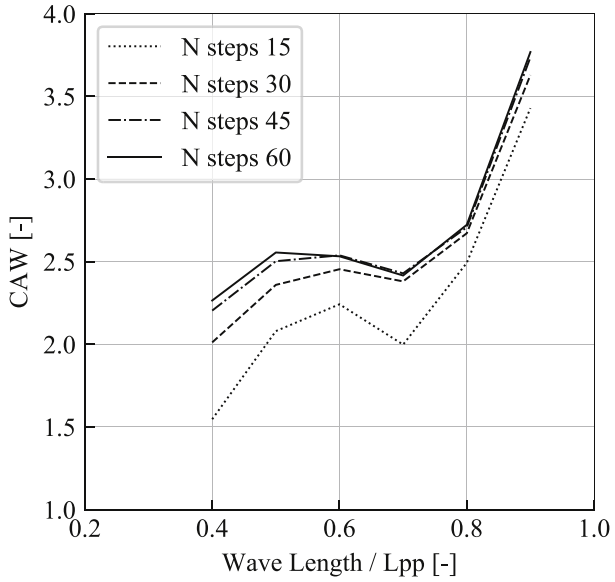


**Fig. 13.** Added resistance coefficient for different number of time steps per fundamental wave.

## 7. Results

The selection of the mesh and the time step size was discussed in Sections 5.4 and 6. The comparison with experimental data is presented in this section. The experimental conditions are reported in Section 4. Three different runs were performed in the towing tank and are visible in the following figures.

For a correct estimation of the added resistance, it is important that the motions are evaluated correctly. In Figs. 15 and 16 the comparison for heave and pitch is shown. Simulated heave and pitch match extremely well the experimental data in the small waves range. For longer waves, a very good agreement can still be seen although heave and pitch are slightly overpredicted.

In Fig. 17 it is possible to see the comparison between the simulated

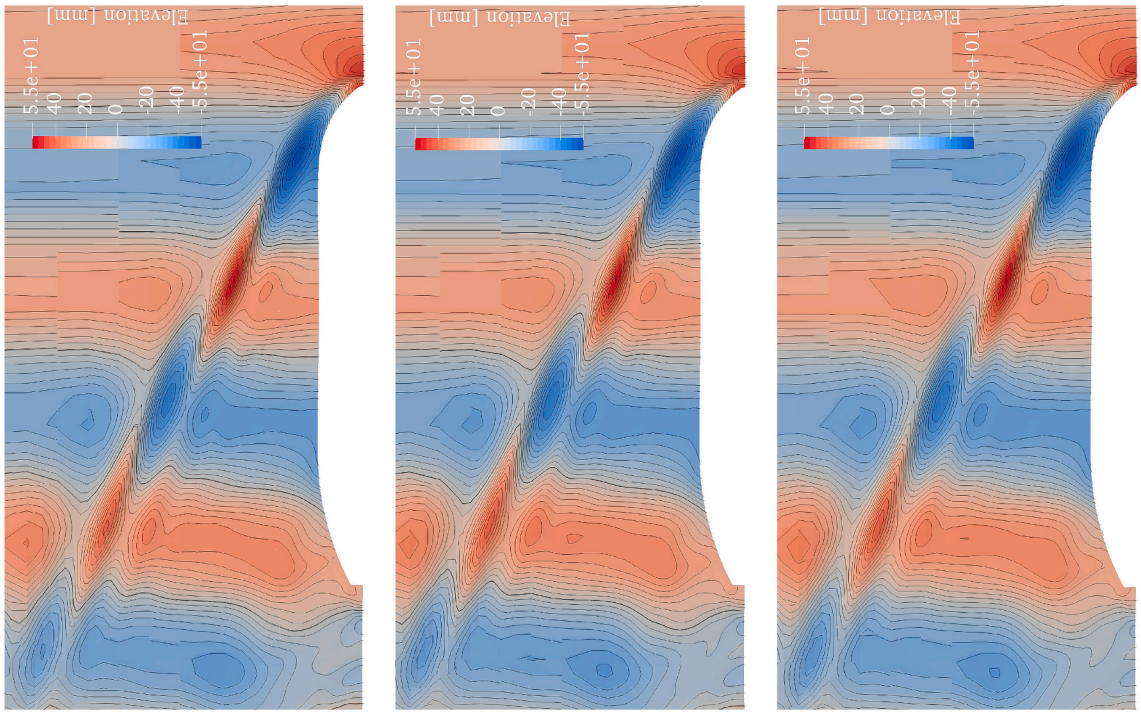


(a) 30 N steps for $\lambda = 0.5 \cdot L_{pp}$ (b) 45 N steps for $\lambda = 0.5 \cdot L_{pp}$ (c) 60 N steps for $\lambda = 0.5 \cdot L_{pp}$

**Fig. 14.** Contour plots for $\lambda = 0.5 \cdot L_{pp}$ for different sizes of the time step and $Fn = 0.142$.

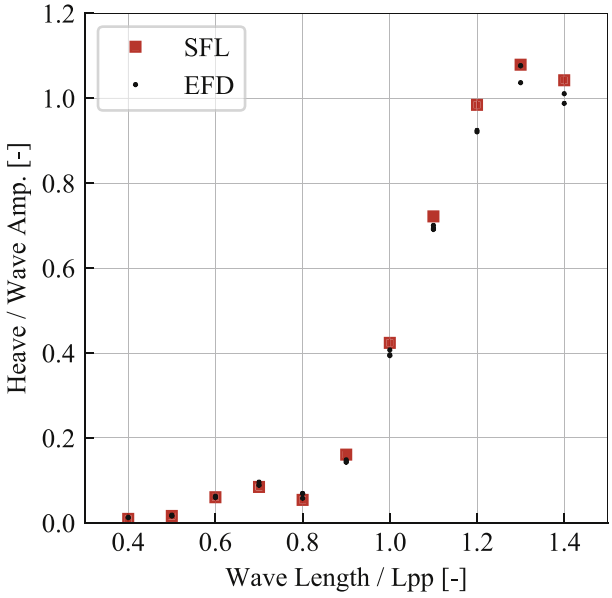


**Fig. 15.** Non-dimensional heave for the KVLCC2 hull at $Fn = 0.142$.

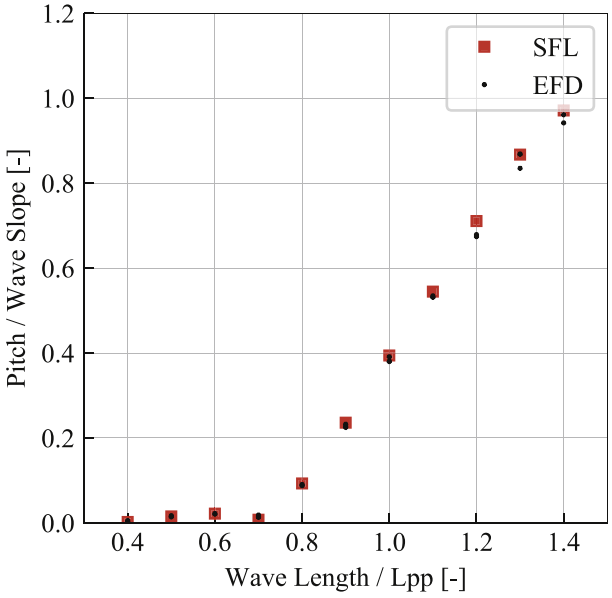


**Fig. 16.** Non-dimensional pitch for the KVLCC2 hull at $Fn = 0.142$.

added resistance coefficient from the current fully nonlinear potential flow and the ones obtained with model tests and from other simulations available in literature. The other methods used for comparison are: a linear potential flow presented in Hizir et al. (2019), a partially nonlinear potential flow method and an Euler method presented in Seo et al. (2014) and an URANS method presented in Sadat-Hosseini et al. (2013). As can be seen, except for the linear potential flow method, there is a general good agreement between the current work and the other computations and the model test results, especially for waves longer than $\lambda = 1.0 \cdot L_{pp}$. For short waves, there is a higher scatter in the results. Since the forces in waves are closer in value to the one obtained in calm water, even a small difference will result in a bigger discrepancy in the added resistance coefficient. It must be pointed out also that the wave steepness for the present method was the same as in the experiments ($s_w = 1/50$ for $\lambda \leq 0.9$ and $s_w = 1/100$ for $0.9 < \lambda \leq 1.4$), while the steepness for the other methods was $s_w = 1/60$ for the linear potential flow, $s_w = 1/40$ for the partially nonlinear potential flow and Euler method and $s_w = 1/53$ for the URANS method.

## 8. Discussion

In the work presented here, a fully nonlinear potential flow boundary

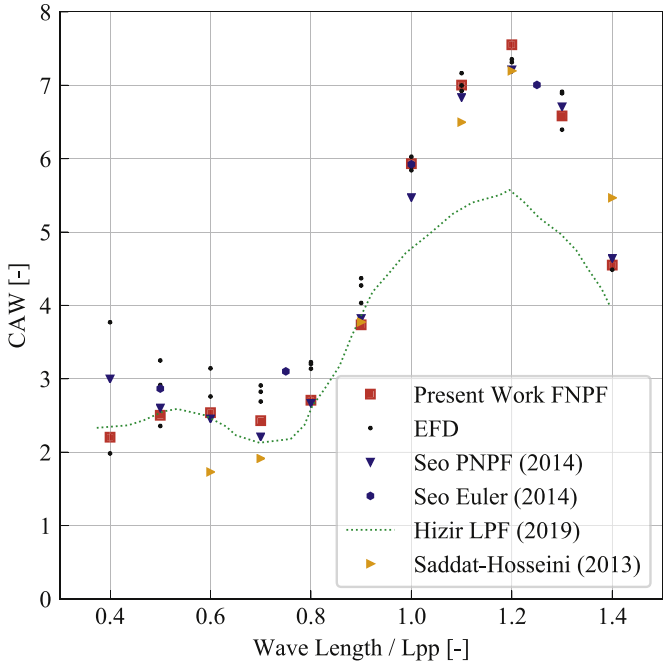


**Fig. 17.** Added resistance coefficient for the KVLCC2 hull at $Fn = 0.142$.

element method has been used to evaluate added resistance, heave and pitch for the KVLCC2 tanker in head waves. In this context, fully nonlinear means that the method is expected to capture all nonlinearities that are not due to viscosity. The fully nonlinear kinematic and dynamic boundary conditions are applied on the free surface. The wavy intersection between the hull and the free surface is computed and updated in each time step. Geometrical nonlinearities due to the variation of the water plane area are captured. Interactions between incoming waves, diffraction waves, radiation waves and waves due to the speed of the hull are all captured simultaneously in the total velocity potential.

Methods based on the potential flow approximation are however limited to cases where the influence of viscous effects on the area covered by potential flow are expected to be small. A thin boundary layer developing along a hull has a small effect, while the flow downstream of a blunt stern is dominated by viscous effects and cannot be captured accurately by potential flow.

The results presented here were in good agreement with experimental results and with other methods. Nevertheless, it must be pointed out that only small wave steepness values were used for the simulations and the Froude number is not high. When stepping outside of these conditions, problems could arise due to the potential flow assumption. When it comes to the speed of the hull, the current method is not able to simulate pre-planing and planing regimes: in order to obtain the lift, vortices or prescribed flow would have to be included. Another problem that would arise when simulating a planing hull is the presence of sprays and breaking waves produced by the hull, which cannot be replicated by a potential flow method. Similarly to the sprays and breaking waves produced by the hull, too steep waves cannot be simulated either, since they would result in breaking waves and overturning waves.

## 9. Conclusion

In the paper presented here an unsteady fully nonlinear potential flow method is used to evaluate added resistance and vertical motions for the KVLCC2 tanker hull. Numerical results are compared with experiments. The code uses an adaptive grid refinement which allows for a finer mesh around the hull and a coarser representation of the domain further away, increasing accuracy and efficiency of the computations. This is well paired with the nonlinear decomposition of the velocity potential used in the code which further increase the efficiency: since the potential of the incoming waves is known, coarser representation of the domain can be used away from the hull. In order to reduce the computational time, a Barnes-Hut algorithm is implemented in the code. Furthermore, a formulation for the acceleration potential is introduced in order to reduce the numerical error deriving from the differentiation of the velocity potential in the Bernoulli's equation.

Before comparing the numerical results with the experimental data, a grid dependency study was performed, aimed at finding the best compromise between computational effort and accuracy of the results. As can be seen in the figures presented in Section 5, small variations in the solution can be observed, excluding cases 1, 2 and 4 where not enough panels are used to discretize the domain, especially around the waterline for cases 1 and 2. To achieve a good agreement with experimental data, the resolution of the grid has to be at least as fine as the one used for case 7. Increasing the number of panels though, the computational time per encounter period rises with a factor of almost 2 between two consecutive refinements.

Before performing the comparison with the experimental data, a time step dependency study was performed. It was noted that this had an influence on short waves and the difference between different time step sizes diminished with increasing wave length. Although contour plots did not show any major difference between the different possibilities, a clear convergence was visible when looking at the added resistance coefficient.

Finally, the numerical results for heave and pitch match very well with the experimental data for all wave lengths. The added resistance coefficient was compared with experimental results and with other numerical methods, including linear potential, partially nonlinear potential flow, Euler method and URANS, and a general good agreement is found. For shorter waves there is a bigger discrepancy but the added resistance is still comparable to experimental results and the other methods. For this range, even a small deviation in the estimation of the force could lead to bigger differences in terms of added resistance coefficient. Furthermore, different numerical methods used different waves steepness, as presented in Section 7, making it hard to compare the results. It is not possible to conclude from this comparison that any method is significantly superior to the others for the KVLCC2 case.

When looking at the total computational time, it must be kept in mind that several encounter periods are simulated: they range between 44 for the case $\lambda = 1.4 \cdot L_{pp}$ up to 100 for the shortest waves. Nevertheless, there is room for improvement in terms of computational time when it comes to the code itself. First of all, the code has not been optimized yet as far as computational efficiency is concerned. Another key aspect to keep in mind is that with the current method for the acceleration potential, one Laplace problem is solved for each degree of freedom. There are more efficient ways to deal with this issue which will be implemented in the future. On the other hand, the pre-process phase is very efficient: there is an automatic mesh generator within the program, which allows to create the mesh on the hull at the first time step and which continues to mesh the free surface during every time step.

## CRediT authorship contribution statement

**Francesco Coslovich:** Investigation. **Martin Kjellberg:** Software, Validation, Writing – review & editing. **Magnus Östberg:** Software, Validation, Writing – review & editing. **Carl-Erik Janson:** Supervision, Funding acquisition, Writing – review & editing.

## Declaration of competing interest

The authors declare that they have no known competing financial interests or personal relationships that could have appeared to influence the work reported in this paper.

## Acknowledgment

This research is funded by Chalmers University of Technology. The experimental results were provided by SSPA Sweden AB.

## References

Barnes, J., Hut, P., 1986. A hierarchical O(N log N) force-calculation algorithm. Nature 324, 446–449. https://doi.org/10.1038/324446a0.

Ducrozet, G., Bingham, H.B., Engsig-Karup, A.P., Ferrant, P., 2010. High-order finite difference solution for 3D nonlinear wave-structure interaction. J. Hydrodyn. 22, 225–230. https://doi.org/10.1016/S1001-6058(09)60198-0, 10.1016/S1001-6058(09)60198-0.

Engsig-Karup, A., Bingham, H., Lindberg, O., 2009. An efficient flexible-order model for 3D nonlinear water waves. J. Comput. Phys. 228, 2100–2118. https://doi.org/10.1016/j.jcp.2008.11.028.

Faltinsen, O., Minsaas, K., Liapis, N., Skjrdal, S., 1980. Prediction of resistance and propulsion of a ship in a seaway. In: Proceedings of the 13th Symposium on Naval Hydrodynamics.

Gerritsma, J., Beukelman, W., 1972. The excess resistance of a ship in rough seas. Int. Shipbuild. Prog. 19, 285–293. https://doi.org/10.3233/ISP-1972-1921701.

Guha, A., Falzarano, J., 2015. The effect of hull emergence angle on the near field formulation of added resistance. Ocean. Eng. 105, 10–24. https://doi.org/10.1016/j.oceaneng.2015.06.012.

Hizir, O., Kim, M., Turan, O., Day, A., Incecik, A., Lee, Y., 2019. Numerical studies on non-linearity of added resistance and ship motions of KVLCC2 in short and long waves. International Journal of Naval Architecture and Ocean Engineering 11, 143–153. https://doi.org/10.1016/j.ijnaoe.2018.02.015.

Joncquez, S., Bingham, H., Andersen, P., 2008. Validation of added resistance computations by a potential flow boundary element method. In: Proceedings of the 27th Symposium on Naval Hydrodynamics.

Joosen, W., 1966. Added resistance of ship in waves. In: Proceedings of the 6th Symposium on Naval Hydrodynamics.

Kang, C.G., Gong, I.Y., 1990. A numerical solution method for three-dimensional nonlinear free surface problems. In: Proceedings of the 18th Symposium on Naval Hydrodynamics.

Kim, K.H., Seo, M.G., Kim, Y., 2012. Numerical analysis on added resistance of ships. Int. J. Offshore Polar Eng. 22, 21–29. https://doi.org/10.1016/j.oceaneng.2010.12.007.

Kjellberg, M., Janson, C.E., Contento, G., 2011. A nested domains technique for a fully-nonlinear unsteady three-dimensional boundary element method for free-surface flows with forward speed. In: Proceedings of the 21st International Offshore and Polar Engineering Conference, pp. 673–679.

Kjellberg, M., Janson, C.E., Contento, G., 2012. Fully nonlinear potential flow method for three-dimensional body motion. In: Proceedings of NAV 2012 the 17th International Conference on Ships and Shipping Research.

Liu, S., Papanikolaou, A., Zaraphonitis, G., 2011. Prediction of added resistance of ships in waves. Ocean. Eng. 38, 641–650. https://doi.org/10.1016/j.oceaneng.2010.12.007.

Longuet-Higgins, M.S., Cokelet, E.D., 1976. The deformation of steep surface waves on water - I. A numerical method of computation. In: Proceedings of the Royal Society A: Mathematical, Physical and Engineering Science, Proc. R. Soc. Lond. A.

Maruo, H., 1957. The excess resistance of a ship in rough seas. Int. Shipbuild. Prog. 4, 337–345. https://doi.org/10.3233/ISP-1957-43501.

Moctar, B., Kaufmann, J., Ley, J., Oberhagemann, J., Shigunov, V., Zorn, T., 2010. Prediction of ship resistance and ship motions using RANSE. In: Proceedings of the Gothenburg Workshop on Numerical Ship Hydrodynamics, pp. 481–491.

Mola, A., Heltai, L., DeSimone, A., 2017. Wet and dry transom stern treatment for unsteady and nonlinear potential flow model for naval hydrodynamics simulations. J. Ship Res. 61, 1–14.

Sadat-Hosseini, H., Wu, P.C., Carrica, P.M., Kim, H., Toda, Y., Stern, F., 2013. CFD verification and validation of added resistance and motions of KVLCC2 with fixed and free surge in short and long head waves. Ocean. Eng. 59, 240–273. https://doi.org/10.1016/j.oceaneng.2012.12.016.

Seo, M.G., Yang, K.K., Park, D.M., Kim, Y., 2014. Numerical analysis of added resistance on ships in short waves. Ocean. Eng. 87, 97–110. https://doi.org/10.1016/j.oceaneng.2014.05.011.